Sulfobetaine-based ultrathin coatings as effective antifouling layers for implantable neuroprosthetic devices

Jolan Wellens [1], Olivier Deschaume[1], Tristan Putzeys[1,3], Samuel Eyley[2], Wim Thielemans[2], Nicolas Verhaert[3,4], Carmen Bartic[1,*]

[1]Laboratory for Soft Matter and Biophysics, Dept. Physics and Astronomy, KU Leuven, Celestijnenlaan 200D, 3001 Leuven, Belgium.

[2]Sustainable Materials Lab, Department of Chemical Engineering, KU Leuven, campus Kulak Kortrijk, Etienne Sabbelaan 53, 8500 Kortrijk, Belgium.

[3]Experimental Oto-rhino-laryngology research group, Dept. Neuroscience, KU Leuven, Herestraat 49, 3000 Leuven, Belgium.

[4]Department of Otorhinolaryngology, University Hospitals Leuven, Herestraat 49, 3000 Leuven, Belgium.

*Corresponding author. Email address: carmen.bartic@kuleuven.be

1. Introduction

Neural stimulation devices such as cochlear implants (CI), deep brain stimulators, and spinal cord stimulators, are frequently used in surgical therapies for neurological conditions such as hearing loss, Parkinson's disease, or chronic pain (Edwards et al., 2017). These devices alleviate symptoms by transferring electric charge to nervous system tissues. However, the foreign body response (FBR) following implantation with inflammation and resulting fibrotic encapsulation of neural implant electrode arrays, remains a significant challenge for the therapeutic efficacy of these devices (Carnicer-Lombarte et al., 2021)(Kolaya and Firestein, 2021). FBR can lead to tissue damage, resulting in additional functionality loss – for instance, loss of residual low-frequency hearing for CI recipients (Quesnel et al., 2016)(Zhang et al., 2015). Also, device encapsulation by fibrous tissue increases the electrode-tissue interface impedance and, consequently, the stimulation thresholds, with the risk of further tissue damage and undesired neighboring tissue stimulation (such as facial nerve stimulation for CI) or even rendering the implant ineffective. High stimulation pulse rates are hypothesized to improve speech recognition in CI users as the temporal waveform of incoming sound can be more closely approximated (Arora, 2012)(Riss et al., 2016), but as a result of increased impedance values, increasing stimulation pulse widths are often necessary (Neuburger et al., 2009), resulting in lower stimulation pulse rates. Additionally, fibrosis and especially new bone formation can cause significant problems for reimplantation. Except for histological investigation, fibrosis is typically measured through changes in the electrode impedance, given the good correlation between impedance increase and fibrosis level (Wilk et al., 2016).

The main treatment for inflammation and resulting fibrosis has been the administration of anti-inflammatory steroidal drugs. However, long-term, non-specific administration of these steroids is contraindicated (Upadhye and Kumbhare, 2018). The local delivery of anti-inflammatory steroids such as dexamethasone via drug-eluting implants is another investigated approach for controlling inflammation and fibrosis, and it was proven effective in reducing fibrosis shortly after implantation (Lentz et al., 2022). However, this effect is often temporary (Stathopoulos et al., 2014) and high-release

bursts of dexamethasone are hypothesized to cause cellular damage and increase hearing thresholds (Wilk et al., 2016).

Making implants smaller, thinner, and more flexible helps reducing the acute inflammatory responses caused by insertion trauma, but does not prevent the body's innate reaction to foreign materials (Gwon et al., 2015) (Rebscher et al., 2008)(Risi, 2018).

Various antifouling coatings have been proposed with promising results in reducing inflammatory responses (Liu et al., 2019) by inhibiting the adhesion of proteins, macrophages, and, consequently, the resulting signaling cascade in the foreign body response (Anderson et al., 2008). These coatings attempt to hide the implant from the body's natural defenses. Effective antifouling coatings are typically very hydrophilic, with the most common ones being based on polyethylene glycol (PEG). For proteins to adhere to these hydrophilic coatings, strongly bound water molecules must be displaced, which is not energetically favorable.

Recently, zwitterionic coatings such as carboxybetaine, sulfobetaine, and phosphatidylcholine have emerged as more promising antifouling coatings due to their increased hydrophilic properties. Zwitterionic molecules contain both positively and negatively charged functional groups, interacting with water molecules via ionic solvation, having a lower hydration free energy than PEG, which interacts with water molecules only via hydrogen bonding (Erathodiyil et al., 2020)(Estephan et al., 2011) (Zhang et al., 2019). Therefore, the strongly attached surface water prevents protein adsorption. Additionally, zwitterions have zero net charge and thus do not attract charged proteins via electrostatic interactions. For example, sulfobetaine-based coatings were shown to decrease microglia encapsulation of silicon brain implants (Golabchi et al., 2019)(Yang et al., 2020). Patterned zwitterionic hydrogels based on sulfobetaine and carboxybetaine methacrylate (SBMA/CBMA) have previously been proposed as coatings for CIs (Leigh et al., 2017)(Bennion et al., 2021) and shown to reduce friction forces during insertion and inhibit fibroblast adhesion in vitro.

While previous studies showed the potential of such coatings to reduce encapsulation *in vivo*, most of them were not targeted to the electrodes. Moreover, for stimulating electrodes it is also essential to evaluate the impact of any additional coatings on stimulation-relevant parameters such as charge storage capacity (CSC), charge injection capacity (CIC), or impedance changes in the frequency range relevant for electrical stimulation (1-250 kHz), while optimizing the stability of the layer under electrical stimulation. Dencker et al. investigated the influence of an antifouling electrospun silicone fiber coating for CIs on electrode impedance at 1 kHz and showed almost a doubling of the measured impedance (Dencker et al., 2017). Very recently, the polydopamine (PDA) and sulfobetaine coating described by Golabchi et al., has been applied to cochlear implant-like silicone rods and shown to reduce fibrosis and changes in hearing thresholds up to 4 weeks after implantation in rodents, showing the potential of sulfobetaine based antifouling coatings to prevent CI functionality loss due to FBR (Chen et al., 2022). However, the coating influence on the platinum/iridium (Pt/Ir) electrodes was not characterized (only single frequency impedance measurements were performed and revealed an acceptable increase in impedance after coating of the >200 nm thick sulfobetaine layer).

In vivo impedance changes measured on CI electrode arrays have been attributed both to protein and cell adhesion (Harris et al., 2022)(Duan et al., 2004). Protein and biomolecule-induced biofouling has been shown to have a major influence on the stimulation properties of Pt electrodes *in vitro* (Harris et al., 2021), and antifouling coatings can in principle inhibit biofouling and thus its influence on stimulation properties. In vitro studies have shown that fibroblasts induce impedance increases on gold electrodes (Li et al., 2010)(Vatsyayan et al., 2011), and so do glial cells on iridium oxide neural implants (Frampton et al., 2010), however, to the best of our knowledge, these studies have not yet

been performed on CI electrode arrays with Pt as an electrode material, nor has the mitigation of cell-induced impedance changes by antifouling coatings been investigated *in vitro*.

In this work, we have studied the antifouling properties of an ultra-thin coating (i.e., ~ 6 nm) consisting of polydopamine, polyethyleneimine (PEI), and a copolymer, Poly(SBMA-co-MA), of SBMA and methacrylic acid (MA), which can be readily applied to electrode arrays of existing neural implants due to the good adhesive properties of the base PDA layer and to the simple modification process consisting of dip coating and self-assembly. This coating presents stable protein and cell-repellent properties evaluated *in vitro* in cell cultures, for at least 31 days and under electrochemical stimulation conditions. Additionally, we show that the layer does not influence stimulation-relevant electrochemical properties of Pt electrodes in pure and protein-containing physiological solutions, specifically phosphate-buffered saline (PBS), and diluted fetal bovine serum (FBS). However, in cell culture, by preventing fibroblast adhesion, the SBMA-coated electrodes display much smaller impedance changes compared to non-coated electrodes, in the frequency range relevant for CI stimulation. Given the high cost of medical devices, we performed most of the experiments on test devices made by microfabrication using materials with compositions and electrode geometries similar to those of clinical devices. However, at last, we applied the SBMA coating onto CI electrode arrays kindly provided by Cochlear Ltd. and observed that both fibroblast adhesion and the accompanying impedance changes are suppressed in cell cultures *in vitro*. Moreover, the impedance changes for occurring for uncoated CI electrode arrays are several times higher compared to microfabricated planar Pt electrodes. SBMA-coated CI electrode arrays showed stable impedance values in cell cultures *in vitro* and therefore, such coatings should be further considered for *in vivo* studies of biofouling, inflammation, and fibrosis related to the use of electrical neuromodulation implants.

2. Materials and methods

The used reagents, instruments, and detailed experimental steps are provided in the supporting information (SI).

3. Results and discussion

3.1. Characterization of antifouling layers

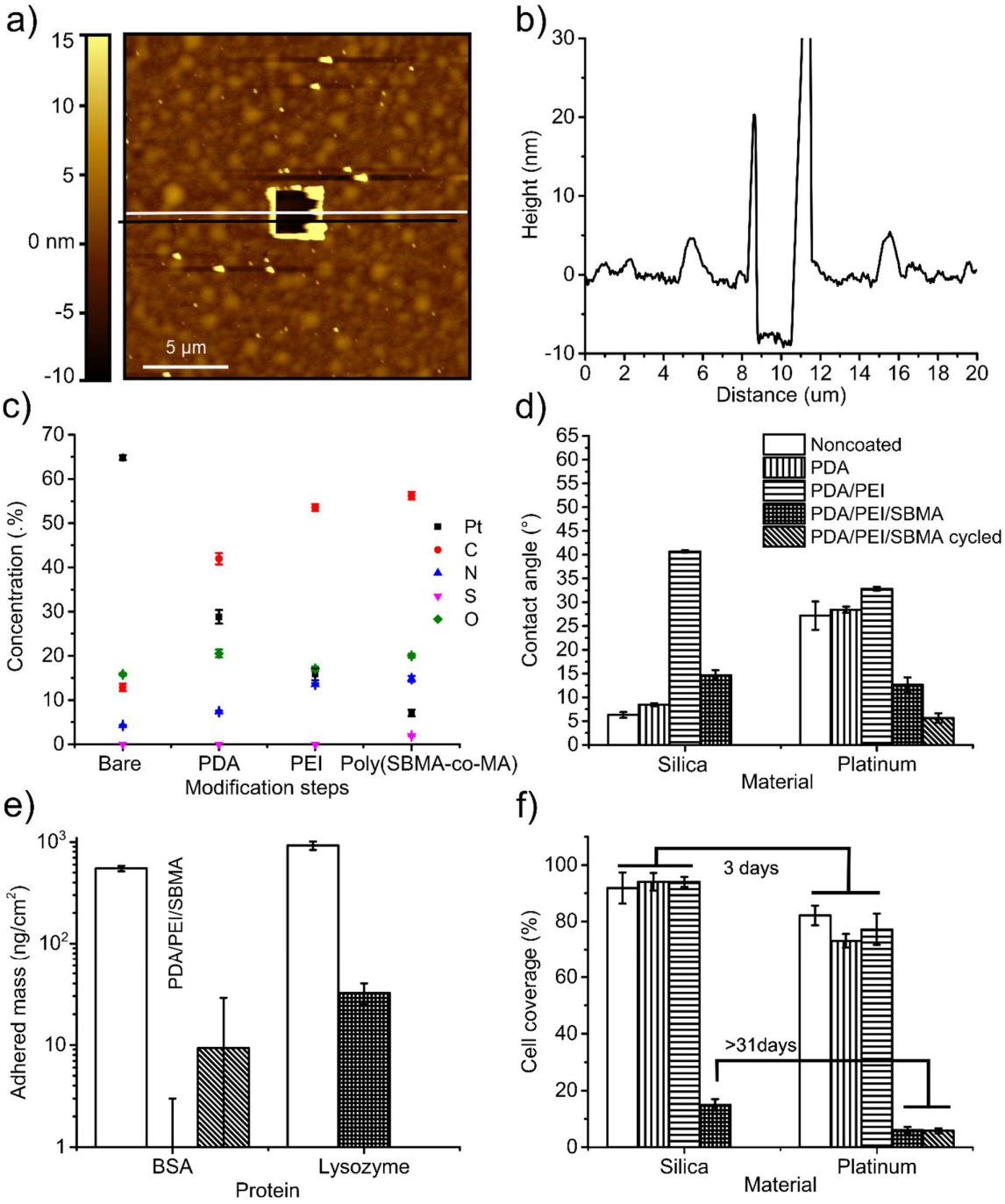

Figure 1. *Characterization and antifouling properties of PDA/PEI/SBMA coating. (a) AFM image of the antifouling coating in dry conditions on a pt substrate with scratched square in the center. (b) Height profile along the white line in a. (c) Elemental composition of coating on Pt substrates, equivalent homogeneous concentration with standard deviation (n = 3, n is number of replicates) was derived from XPS. (d) Contact angle values with standard deviation measured on silica and Pt after each surface modification (n = 3). Legend also applies to figure e and f. (e) Adsorbed protein (BSA and lysozyme)*

mass on Pt from a 10 mg/ml solution with standard error, extracted from QCM measurements (n = 3). The column for BSA adsorption on PDA/PEI/SBMA is not visible in the log scale due to a slightly negative value, the absolute value is lower than the detection limit due to the QCM noise. (f) Surface coverage by 3T3 fibroblasts with standard deviation after each surface modification step on silica and Pt (n = 3).

The developed antifouling coating consists of 3 layers. Firstly a base layer of PDA, which has been shown to have good adhesive properties on a wide range of substrates (Ryu et al., 2018). PEI then binds to the dopamine layer via its amine groups due to Michael-type or Schiff-base reactions (Liu et al., 2014). This leads to a surface rich in amine groups to which Poly(SBMA-co-MA) can bind via its carboxyl group on MA via carbodiimide chemistry which results in the formation of an amide bond (Thermo Fisher, 2012). A schematic of the layer can be found in the SI in **Figure S1**. We will refer to the different layer deposition steps as PDA, PDA/PEI, and PDA/PEI/SBMA.

To investigate the morphology and thickness of the PDA/PEI/SBMA coating, intermittent contact mode atomic force microscopy (AFM) measurements were performed. A representative image can be seen in **Figure 1a** along with a height profile in **Figure 1b**. The coating was found to have an average thickness of 6 ± 1.7 nm under dry conditions (Extra information on data analysis is found in Section 1.6 of SI). Ultra-thin coatings are essential for preserving the electrode impedance. In our case, the coating thickness mainly depends on that of the underlying polydopamine layer, which is a function of the immersion time (Gao et al., 2014), and poly(SBMA-co-MA) polymer chain length, respectively. We have also tested longer immersion times for the PDA deposition solution (i.e., 3 hours – data not shown) and higher molecular weight poly(SBMA-co-MA) polymers, but these experiments showed that thicker coatings (i.e., 10 nm dry, 20 nm in water on silica) do not have significantly better antifouling/cell repellent properties while yielding significantly higher Pt electrode impedance values (data not included).

Elemental analysis following the different modification steps was performed with X-ray photoelectron spectroscopy (XPS) and the homogeneous equivalent concentration can be seen in **Figure 1c** for Pt substrates. These data reveal that the dopamine deposition process leads to an increase in the contents of carbon (C) (+ 29 %), nitrogen (N) (+ 3.1%), and oxygen (O) (+ 4.7 %), which are elements present in dopamine, indicating the presence of a dopamine containing layer on top of the Pt substrate. After immersion in PEI, the concentrations of C (+ 11 %) and N (+ 6.2 %) increased, indicating successful conjugation of PEI. Poly(SBMA-co-MA) modification further increased the concentration of both C (+ 3 %) and more importantly sulfur (S) (+ 2 %), indicating the presence of this polymer on the surface. The detected Pt concentration decreased after each modification step, by respectively - 36 %, - 13 %, and – 9 %, indicating a gradual buildup of an organic layer on top of the Pt substrate. The presence of complete overlayers on the Pt substrate is also indicated by the increase in the intensity of the loss background to the left of the Pt 4f peak, caused by the scattering of Pt 4f electrons by increasing amounts of material deposited on the Pt substrate (see **Figure S3**) (Tougaard, 2021).

The different steps of constructing the antifouling layer (PDA, PDA/PEI, and PDA/PEI/SBMA) were characterized by contact angle (CA) measurements. As can be seen in **Figure 1d**, the addition of the PDA layer barely changes the CA, while after the addition of PEI, the surface becomes significantly less hydrophilic. After SBMA binding, the surface hydrophilicity increased again, indicating that indeed a hydrophilic polymer layer is attached. Pt also becomes significantly more hydrophilic after the coating process. The hydrophilicity of the PDA/PEI/SBMA coated Pt (CA of 12.6 ± 1.6 °) is similar to that of coated silica (14.6 ± 1.1 °). To evaluate the possible degradation of the antifouling coating as a result of the electrical stimulation, the SBMA-coated Pt electrodes were subjected to a voltage cycling protocol of 100 cycles between potentials of -0.6 V and 0.9 V at a scan speed of 2000 mV/s in PBS. These potentials are the safe stimulation limits for Pt electrodes, and it is assumed that during cochlear

stimulation these are not exceeded. We refer to substrates exposed to this protocol as "voltage cycled" in further discussions. As can be seen in **Figure 1d**, the CA after voltage cycling was even lower (i.e., 5.6 ± 1.0 °) than before.

3.2. Protein and cell repellence

Quartz crystal microbalance (QCM) data show that the SBMA coating reduces the adhesion of both positively charged lysozyme and negatively charged bovine serum albumin (BSA) proteins as compared to unmodified substrates by 96 ± 0.8 % for lysozyme and for BSA the adhered mass was under the detection limit of the QCM (<7.6 ng/cm^2) (see **Figure 1e)**. The surface coverage of lysozyme (32 ± 7.6 ng/cm^2) is slightly higher than for BSA (< 7.6 ng/cm^2), which can be explained by the small negative net charge of the copolymer, consisting of both neutral SBMA and negative MA subunits, attracting more the positively charged lysozyme. Also, the coated QCM chips were subjected to voltage cycling as described above and BSA adhesion was measured afterward. A slight increase in the average adhered BSA mass was noticed (9±20 ng/cm^2) but it was not significantly different from the non-cycled chip indicating that the coating is stable under electrical stimulation conditions (p-value = 0.55 from one-tailed T-test, unpaired, unequal variances).

Fibroblasts and macrophages are the most important cells involved in the foreign body response. Fibroblasts are attracted by macrophages and create a collagenous fibrous capsule around the implant effectively isolating it from its environment (Chandorkar et al., 2019) (Bas et al., 2015). Preventing their adhesion to the surface of the electrode is thus crucial. Cell repellence was studied for up to a month *in vitro* and the results can be seen in **Figure 1f**. On SBMA-coated silica substrates, the adhesion of 3T3 fibroblasts is significantly reduced compared to the non-coated substrates for the entire measurement period (i.e., 31 days), whereas modifications with PDA or PDA/PEI alone show complete 3T3 cell coverage after only 3 days in culture. The same effect is observed for Pt substrates where the SBMA layer almost completely inhibits cell adhesion. Again, the antifouling coating was tested for potential degradation by voltage cycling, and the cell-repellent behavior remains unchanged. Similar stable cell repellence properties in cell culture conditions have only been reported a few times, such as by Kuang and Messersmith who utilized a base layer consisting of a dopamine-like catechol from which PSBMA was grown through surface-initiated polymerization resulting in a thicker 30 nm layer (Kuang and Messersmith, 2012).

3.3. SBMA-coating influence on electrical properties of Pt electrodes in PBS and FBS

After verifying the protein and cell-repellent properties of the PDA/PEI/SBMA coating, the influence of this film on the electrical properties of Pt electrodes relevant to neural stimulation was tested. For all the tests, microfabricated Pt electrodes with dimensions similar to the ones used in commercial CIs were used (i.e., 250 by 500 µm).

Firstly, the electrochemical behavior of Pt electrodes in PBS was investigated before and after the coating process. The charge injection current, peak-to-peak voltage amplitude (ΔV) and charge storage capacity were derived from the stimulation waveform and cyclic voltammetry (CV) graphs shown in **Figures 2c, d, e, and f** (for detailed explanation see supplementary information section 1.10). High CSC and CIC but low impedance ($|Z|$) and peak-to-peak voltage amplitude are desirable properties for stimulation electrodes, and it is thus important to evaluate changes in these parameters as a result of the applied coating.

$|Z|$, cathodic CSC, ΔV, and CIC barely differ between coated and uncoated electrodes, indicating that the coating had almost no effect on the stimulation properties of Pt electrodes (**Figure 2a**, **Table S2, Table S3**). The only significant differences are a slight increase in CSC at 100 mV/s (from 707 ± 32 μC/cm^2 before to 770 ± 24 μC/cm^2 after coating) and the impedance values at 10 kHz (2.109 ± 0.022 kΩ to 2.151 ± 0.026 kΩ after coating). The cathodic CIC in PBS could not be determined accurately because applying charge pulses higher than 140 μC/cm^2 is not possible with the potentiostat used.

Impedance spectra fitted with a Randles equivalent circuit (**Figure 2a**) were used to extract the solution resistance (R_s), charge transfer resistance (R_{ct}), and a constant phase element (*CPE*). The *CPE* with impedance $Z_{CPE} = \frac{1}{Q_0(i\omega)^n}$ with $0.5 < n < 1$, Q_0 the admittance, and ω the frequency, is often found to better fit the measured spectra than a double layer capacitance (C_{dl}) and this behavior is attributed to surface roughness and non-uniform current distribution (Jorcin et al., 2006).

The antifouling layer lowers the charge transfer resistance from 138 ± 26 MΩ to 39 ± 12.5 MΩ (**Table S4**), which is most likely due to redox reactions involving the coating. Such reduction of the R_{ct} was also seen on thicker (40 nm) polydopamine films, where polydopamine could undergo reversible redox reactions between its hydroquinone, semiquinone, and quinone forms (Kwon et al., 2016)(Wu et al., 2015). An *n* value close to 1 indicates that the CPE behaves as a capacitor. Fitting our data gives a value $n \approx 0.9$ and thus the admittance of the *CPE* element, Q_0, can be seen as the capacitance.

CV graphs of the coated and uncoated electrodes in PBS show little difference both at fast (2 V/s) and slow (100 mV/s) scan rates as can be seen in **Figures 2e** and **2f**.

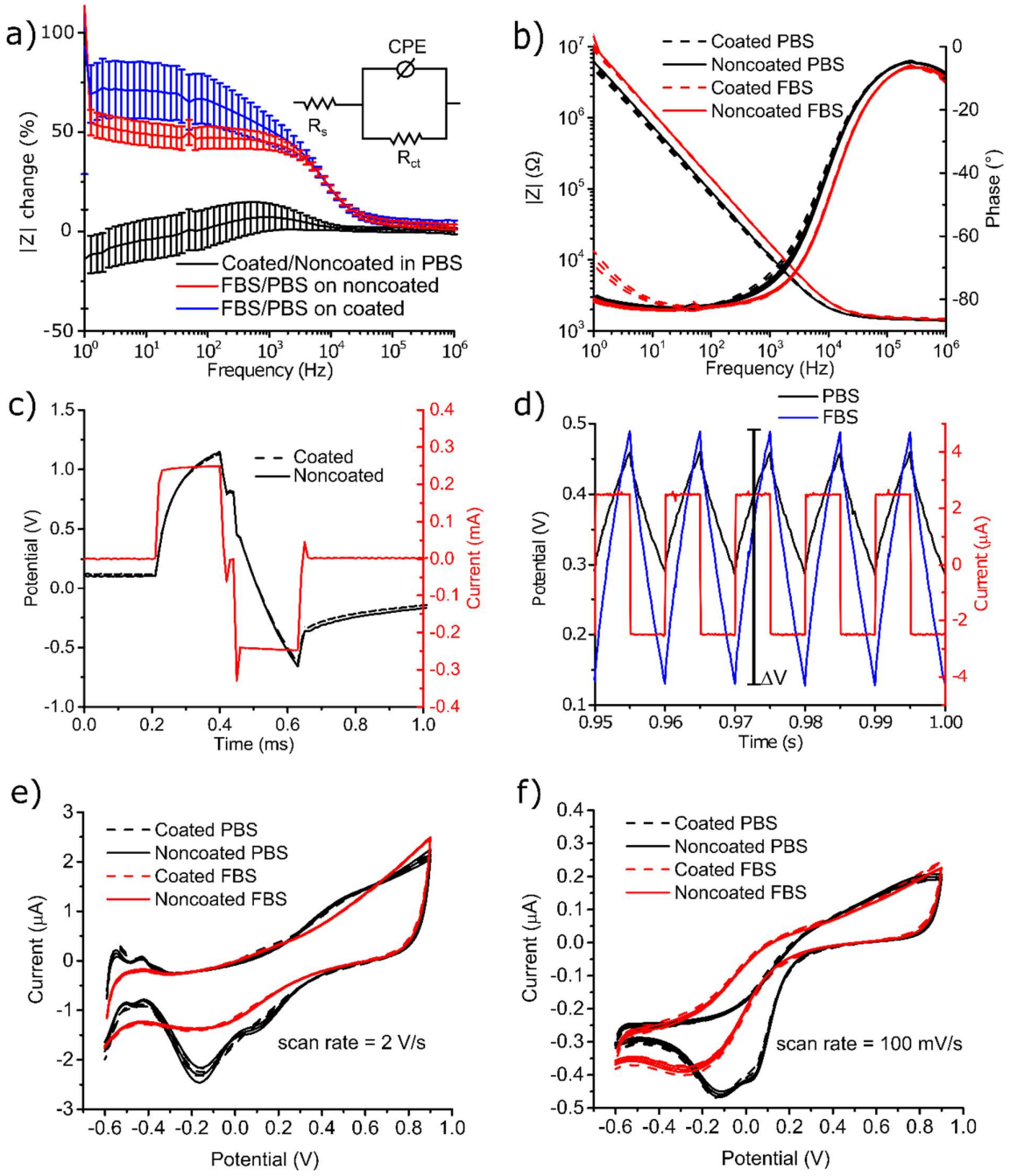

Figure 2. *Characterization of electrochemical properties on Pt electrodes. Coated/Noncoated indicates change as a result of the coating process, and FBS/PBS indicates change as a result of changing measurement solution from PBS to 10% FBS supplemented PBS. (a) Percentual impedance modulus change, (Z_1/Z_2-1)*100%, with standard error (n = 15 - 16). The equivalent circuit used for modeling the impedance spectrum is shown as an inset. (b) Impedance modulus and phase spectrum with standard error (n = 15). (c) Example of voltage transient at 40 µC/cm^2 in 10% FBS on both noncoated and coated electrodes. (d) Example of chronopotentiometry experiment with current pulses of 10 µC/cm^2 in PBS and 10% FBS on the noncoated electrode. (e) And (f) average and standard error of CVs taken at scan speeds of 2000 mV/s and 100 mV/s respectively (n = 20).*

The influence of proteins and other biomolecules (carbohydrates, amino acids, lipids) on the electrical properties of Pt electrodes was tested by performing the same measurements in PBS supplemented with 10% FBS, a solution with a protein concentration of ~4 mg/ml. This is close to the physiological protein concentration in perilymph (i.e., the fluid in the cochlea), of about 2 mg/ml (Lysaght et al., 2011).

Except for the anodic CSC, the electrochemical properties drastically change in a PBS solution supplemented with 10% FBS for both coated and noncoated electrodes. In fast scan CVs, both the Pt oxidation (0.45 V) and reduction (0.05 V) peaks disappear, and a strong decrease of 1 µA in the oxygen reduction peak (-0.15 V) is observed (**Figure 2e**). The peaks associated with hydrogen absorption between - 0.4 V and - 0.6 V disappear as well. Previous research has shown that such changes can be caused by the adsorption of proteins (Farcas et al., 2010) and/or, smaller amino acids such as L-phenylalanine (Wright et al., 2003). At potentials above 0.6 V, the oxidation current increases with 0.5 µA, which can be explained by the oxidation of metabolites, peptides, and amino acids in the FBS (Suprun, 2021)(Dorčák et al., 2013)(Suprun et al., 2016). At slow scan speeds, the Pt oxide reduction peak is no longer observed, and the oxygen reduction peak is smaller and negatively shifted by around -150 mV (**Figure 2f**). Higher oxidation currents above 0.8 V are noticed due to the oxidation of proteins and other molecules present in FBS.

These qualitative changes are also reflected in the CSC, CIC, and ΔV values (**Table 1**). The cathodic CSC is significantly inhibited at both slow and fast scan rates in PBS supplemented with 10% FBS for both coated and uncoated electrodes. For the anodic CSC at both scan rates, no significant difference is seen. The Tukey test shows a difference in the anodic CSC at 100 mV/s between coated and uncoated electrodes in 10% FBS. The ratio of $\Delta V_{FBS}/\Delta V_{PBS}$ is for coated electrodes slightly higher than for uncoated (1.82 vs 1.68 and 1.97 vs 1.85 for anodic or cathodic first respectively). ΔV is also the only parameter for which a significant correlation is found between the changes from PBS to 10% FBS and whether the electrodes are coated/noncoated. For all other parameters, the presence of the coating does not influence the changes due to the addition of FBS. The CIC for both anodic and cathodic first pulses decreases significantly. The ratio CIC_{PBS}/CIC_{FBS} for the anodic first waveform is 1.83 and 1.64 for the coated and uncoated electrodes, respectively. A stronger decrease is noticeable in the cathodic first CIC (i.e., becoming about half of the CIC for anodic first pulses). The decrease in cathodic CIC is most likely due to the lower oxygen reduction, hydrogen (H^+) adsorption, and reduction of Pt oxide which was also noticed in the CV graphs. For the anodic CIC, it can be due to a decrease in Pt oxidation. These results could indicate that using anodic first biphasic pulses when performing stimulations *in vivo* with Pt electrodes might be more suitable.

|Z| mainly changes at frequencies lower than 20 kHz, becoming roughly 1.5 - 1.7 times larger in 10% FBS than in PBS (**Figure 2a**). Again, the presence of the coating does not influence changes due to the addition of FBS. The changes in anodic CIC (decrease of 1.8) and ΔV (increase of 1.8) agree well with the impedance changes at the respective frequencies of their waveforms, 100 Hz = 1/10 ms for ΔV and 2500 Hz = 1/400 µs for CIC.

The fitting parameters from the Randles equivalent circuit to compare PBS and 10% FBS can be seen in **Table 2.** Q_0 decreases to the same value for both electrode types when 10% FBS was added, indicating a decrease in the capacitance and an increase in the impedance of the *CPE* element.

These results indicate that the coating does not inhibit changes in electrochemical properties when exposed to a serum-containing PBS solution, indicating that these changes (Increase in impedance and decrease in CIC, CSC) are likely not caused by the adhesion of proteins to the electrode but by smaller molecules such as peptides, amino acids, or metabolites.

Table 1. *Stimulation-relevant electrochemical properties CSC, ΔV, and CIC in PBS and 10% FBS with average and standard error as calculated from the Tukey test (n = 20, for CIC n = 8). "FBS" indicates measurement was performed in 10% FBS. The asterisk (*) indicates significant differences between pure PBS and FBS/PBS mixture as calculated by comparisons of means via the Tukey test. The letter ϕ indicates significant differences between coated and noncoated electrodes.*

		Anodic		Cathodic	
		Coated	**Uncoated**	**Coated**	**Uncoated**
CSC 2000 mV/s ($\mu C/cm^2$)	PBS	415 ± 4	411 ± 4	562 ± 9 *	555 ± 9 *
	FBS	418 ± 3	413 ± 3	490 ± 5*	491 ± 5*
CSC 100 mV/s ($\mu C/cm^2$)	PBS	790 ± 20	750 ± 20	3460 ± 60*	3480 ± 60*
	FBS	840 ± 20$^{\phi}$	760 ± 20 $^{\phi}$	2920 ± 60*	2900 ± 60*
ΔV (mV)	PBS	189 ± 6*	195 ± 6*	191 ± 5*	195 ± 5*
	FBS	345 ± 6*	328 ± 6*	377 ± 5*	361 ± 5*
CIC ($\mu C /cm^2$)	PBS	92 ± 3*	83 ± 3*	>140*	>140*
	FBS	50 ± 3*	50 ± 3*	26 ± 7*	27 ± 6*

3.4. Influence of fibroblast adhesion on electrode impedance

To investigate the influence of cell adhesion on the stimulation properties of coated and uncoated electrodes, impedance measurements are performed. **Figure 3c** shows a confluent monolayer of 3T3 fibroblasts on uncoated Pt electrodes after 2 days in culture. The presence of this cell layer causes significant changes in the impedance spectrum of the uncoated electrodes. The largest impedance change occurs at frequencies above 1 kHz (i.e., with a peak impedance increase of 1.6 x at 30 kHz – see the red curve in **Figure 3a**), which coincides with the range relevant to electrical stimulation in CIs (see **Figure 3a** and pulse/frequency ranges for different clinical CI devices given in **Table S6**). Similar increased impedance values as a result of fibroblast adhesion were seen in other studies on gold electrodes at a frequency of 10 kHz (pulse width 50 μs) (Newbold et al., 2004). This increase in impedance induced by the cell encapsulation results in the need for higher stimulation voltages to inject the same current values, and, therefore, is not desirable for efficient stimulation purposes. On the other hand, by preventing cell adhesion (Figure 3d), the SBMA coating allows for maintaining stable impedance values for 3 days in cell culture. As this effect is caused by the formation of a dense cell layer on the electrode and, given that the SBMA-coating can inhibit cell adhesion for at least 31 days in vitro, also the impedance remains stable over this period. ~~The impedance on SBMA-coated electrodes thus remains lower than on noncoated electrodes when exposed to fibroblasts, and this should result in more efficient stimulation.~~

The presence of the fibroblast layer is modeled by including an additional parallel RC element with a resistance (R_c) and a capacitance (C_c), the resulting equivalent circuit is shown as an inset in **Figure 3a**. The inclusion of this additional element is only necessary for noncoated electrodes on which fibroblasts were cultured, in all other cases the impedance spectra can be fitted well with the Randles equivalent circuit shown in **Figure 2a**. The fitting parameters can be found in **Table 2**. Similar effects of cell adhesion on electrode impedance values were simulated in computational finite element studies, where impedance values increased at intermediate frequencies and remained constant at low frequencies (Greve et al., 2003).

***Table 2**. Parameters with errors from fitting impedance spectra to equivalent circuit models are seen in **Figures 2a** and **3a** (n = 5 - 12). "Medium" indicates that the impedance is measured in the medium in the absence of cells. "Cells" indicates that the measurement is performed in cell culture medium 2/3 days after cell seeding. CI indicates that measurements are performed on the CI electrode array and not on planar electrodes. Noncoated electrodes required the inclusion of additional circuit parameters R_c and C_c for an optimal fit after cell culture.*

Solution	Surface	R_s (Ω)	R_c (Ω)	C_c (nF)	Q_0 (nS*S^n)	n	R_{ct} (MΩ)	R^2
PBS	**Noncoated**	1450 ± 20	/	/	29 ± 2	0.917 ± 0.004	210 ± 60	0.981
	Coated	1420 ± 20	/	/	36 ± 3	0.897 ± 0.007	40 ± 10	0.981
FBS	**Noncoated**	1480 ± 20	/	/	18 ± 1	0.923 ± 0.003	400 ± 200	0.981
	Coated	1442 ± 7	/	/	18.4 ± 0.4	0.925 ± 0.001	22 ± 2	0.985
Medium	**Noncoated**	1170 ± 20	/	/	14.1 ± 0.2	0.936 ± 0.002	110 ± 60	0.997
	Coated	1210 ± 10	/	/	13.2 ± 0.1	0.944 ± 0.001	79 ± 2	0.996
Cells	**Noncoated**	1260 ± 20	910 ± 70	1.1 ± 0.1	15.1 ± 0.7	0.923 ± 0.006	8 ± 1	0.998
	Coated	1250 ± 50	/	/	12.9 ± 0.4	0.942 ± 0.004	35 ± 8	0.991
CI medium	**Noncoated**	1010 ± 20	/	/	38.5 ± 0.7	0.879 ± 0.002	50 ± 2	0.996
	Coated	960 ± 28	/	/	56 ± 3	0.857 ± 0.001	88 ± 9	0.997
CI cells	**Noncoated**	1360 ± 20	5400 ± 200	0.260 ± 0.01	39 ± 1	0.869 ± 0.003	210 ± 40	0.996
	Coated	910 ± 10	/	/	44 ± 2	0.871 ± 0.001	170 ± 50	0.997

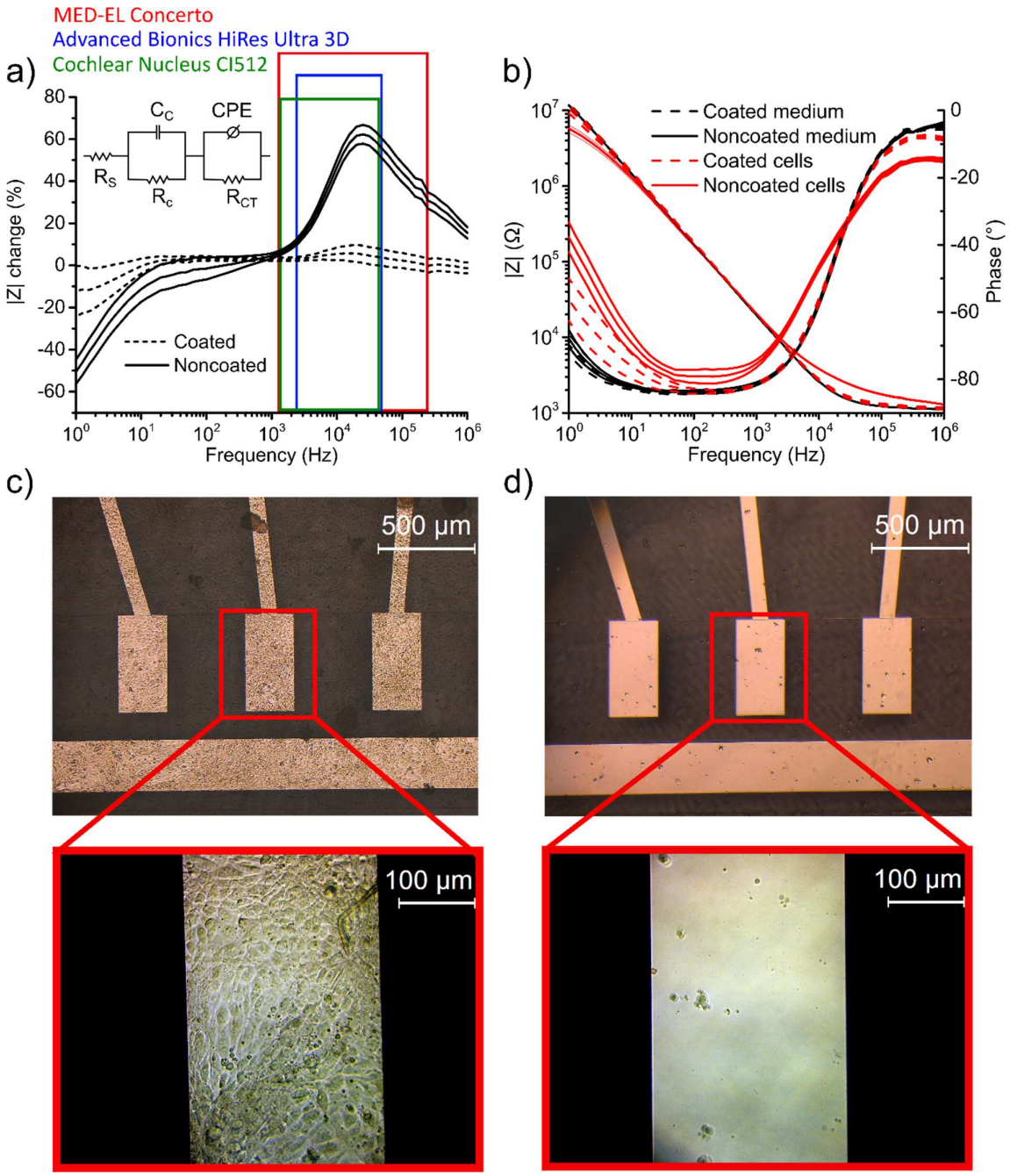

Figure 3. *Influence of 3T3 fibroblast adhesion on coated and noncoated Pt electrodes. (a) Percentual impedance modulus change after culturing of fibroblasts with standard error, the equivalent circuit used to model the influence of additional fibroblast layer is shown as an inset. Colored boxes indicate the relevant frequency range for 3 different commercial CI devices. (b) Impedance modulus and phase spectrum with standard error (n = 11). (c) Noncoated and (d) coated electrodes after culturing of 3T3 fibroblasts for 2 days.*

3.5. Application of SBMA antifouling coating to cochlear implant electrode arrays

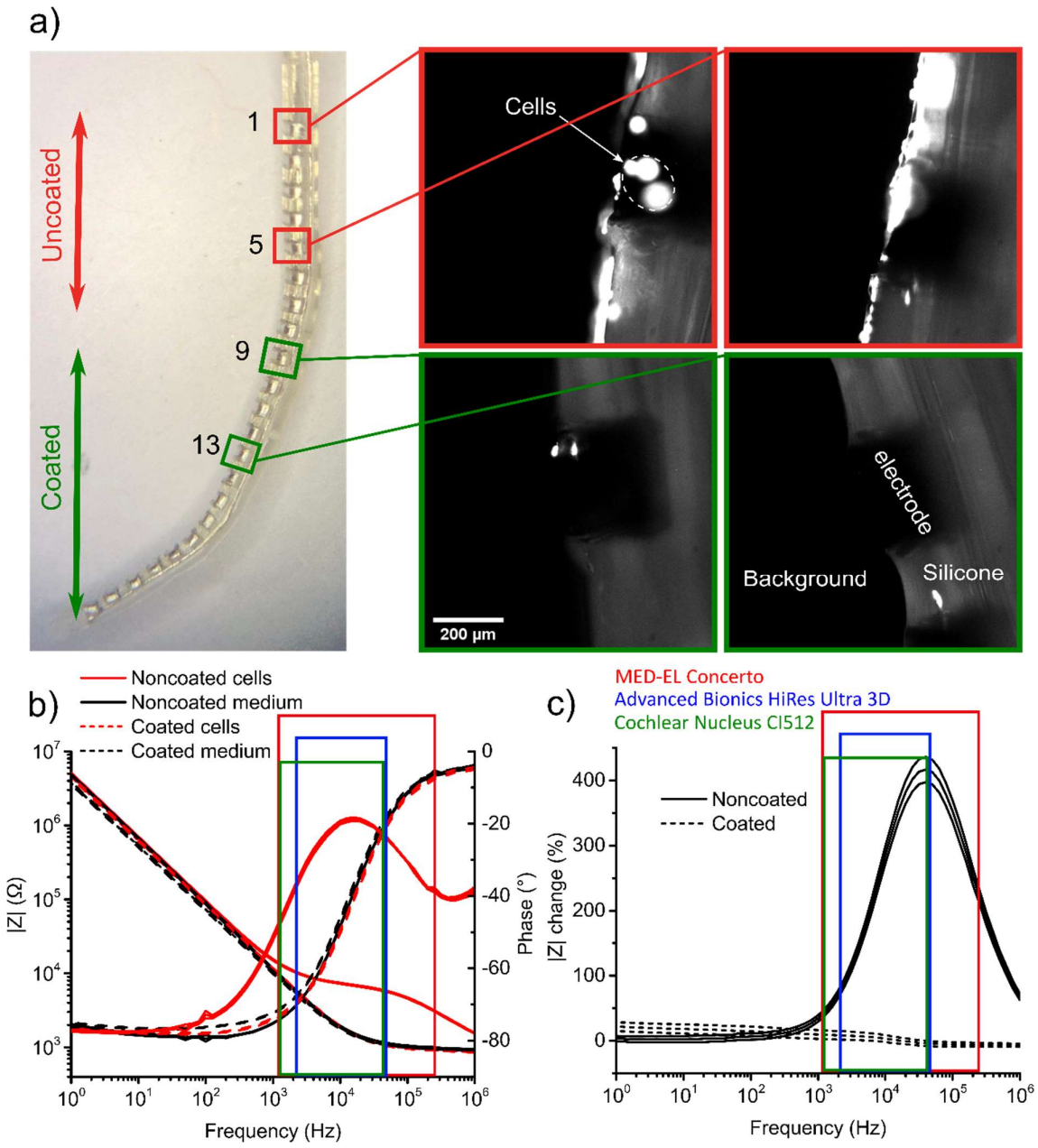

***Figure 4**. Influence of 3T3 cell adhesion on coated and noncoated CI electrode arrays. (a) (left) Image of a CI electrode array. Electrodes 1-7 are not coated and 9-16 are SBMA-coated, numbering starts from the base. (right) Fluorescence microscopy images of the CI electrode array - electrodes 1,5,9,13 are shown. Cells are fluorescently labeled with calcein. (b) Impedance modulus and phase spectrum with standard error of CI electrode in medium and after culturing 3T3 cells for 3 days (n = 7). Colored boxes indicate the relevant frequency range for 3 different commercial CI models. (c) Percentual impedance modulus change with standard error after culturing with 3T3 fibroblasts for 3 days (n = 7).*

The antifouling coatings are also tested on CIs kindly provided by Cochlear ltd. As one can see in **Figure 4a**, the SBMA coating inhibits 3T3 cell adhesion both on the Pt/Ir electrodes of the CI as well as on the silicone passivation, indicating that dip-coating allows to effectively cover both material surfaces. Other microscopy images are included in the SI in **Figure S8**. The influence of 3T3 cells on the impedance spectrum of the non-coated CI electrodes is much more pronounced than for the test planar electrodes as can be seen in **Figures 4b** and **4c.** The non-coated CI electrode impedances are up to 5-fold higher after 3T3 cell attachment, in comparison to planar electrodes where it is only 1.6 -fold, thus showing that cell encapsulation has a much larger and detrimental impact on CI electrode arrays. The cell layer was modeled by including an additional RC component in the equivalent circuit model with a resistance that is 5-fold higher than on planar electrodes (**Table 2**). There are several possible explanations for this. Adherent cells can form multilayers on CI electrodes due to the well-like shape of the device at each electrode contact (Yao et al., 2014). Moreover, the increased roughness of the Pt/Ir electrode surface may enhance cell adhesion. To the best of our knowledge, it is the first time that the influence of cell adhesion on impedance over the entire frequency range has been measured on a CI electrode array. The impedance change at 100 kHz (i.e., increase from 1024 to 4635 Ω) is very similar to that measured *in vivo* after implantation (i.e., 800 to more than 4000 Ω) (Duan et al., 2004) (Harris et al., 2022) indicating that fibroblast adhesion could be the reason for the observed impedance changes *in vivo*. We find that the application of the antifouling coating has a negligible influence on the impedance of the CI electrodes (**Figure 4b**) and no impedance increase is detected following cell culturing on coated CI electrode arrays (**Figure 4c**), resulting in impedance values 5x lower than on a noncoated CI electrode array. The CI electrodes were subjected to the voltage cycling protocol as applied to test electrodes (i.e., 100 cycles, - 0.6 to 0.9 V, 2000 mV/s) before these measurements to investigate the layer stability under electrical stimulation conditions.

4. Conclusions

Preventing implant insulation by fibrotic tissue remains an important challenge for the development of in vivo electrical stimulation devices such as cochlear implants. As shown by our data, an ultra-thin sulfobetaine coating (i.e., ± 6 nm) applied to electrode arrays allows for maintaining a stable electrode impedance in 3T3 fibroblast cultures in vitro, by preventing cell adhesion for a period of at least 31 days. This coating consisting of PDA, PEI, and Poly(SBMA-co-MA), resists protein adhesion and completely inhibits fibroblast attachment *in vitro*. Moreover, when applied to CI electrode arrays, these could maintain impedance values 5 x lower than uncoated CI electrode arrays, in the frequency range relevant for CI stimulation. Additionally, when evaluating the electrochemical properties relevant to electrical stimulation (Impedance, Charge storage capacity, charge injection capacity), we found that the coating maintained its protein and cell-repellence properties and did not negatively impact the stimulation-relevant electrochemical properties of Pt and Pt/Ir electrodes. These *in vitro* results suggest that the investigated coating, while having no obvious detrimental effects on the electrical performance, could help improve the CI performance *in vivo*, by preventing cell encapsulation-induced impedance changes. Therefore, it should be considered for long-term in vivo testing, to evaluate its stability and potential effects on neighboring tissues.

CRediT authorship contribution statement

Jolan Wellens: Conceptualization, Methodology, Validation, Formal analysis (all data except XPS), Investigation (all experiments except XPS/AFM), Data Curation, Writing – Original Draft, Visualisation. **Olivier Deschaume:** Investigation AFM, Writing – Review & Editing. **Tristan Putzeys:** Software, Writing – Review & Editing, Supervision. **Samuel Eyley:** Investigation and Formal analysis XPS, Review & Editing. **Wim Thielemans:** Resources and Funding acquisition, Review & Editing. **Nicolas Verhaert:**

Writing – Review & Editing, Funding acquisition. **Carmen Bartic:** Conceptualization, Writing – Review & Editing, Resource and Project coordination, Funding acquisition.

Declaration of competing interests

The authors declare that they have no known competing financial interests or personal relationships that could have appeared to influence the work reported in this paper.

Acknowledgments

J. Wellens acknowledges the financial support by the Fonds Wetenschappelijk Onderzoek, Belgium (FWO-SB doctoral grant 1S64622N). N. Verhaert, C. Bartic and O. Deschaume acknowledge the support of the FWO research grant G088619N. T. Putzeys is funded by Flanders Innovation and Entrepreneurship (Grant IWT155047). N. Verhaert has a senior clinical investigator fund of Research Foundation Flanders (FWO Grant 1804816N). S. Eyley, and W. Thielemans also acknowledge financial support from KU Leuven grant C14/18/061 and FWO Grant G0A1219N. The authors are grateful to Cochlear Limited for providing the Cochlear Implant electrode arrays and associated electrical connectors and adapters.

References

Anderson, J.M., Rodriguez, A., Chang, D.T., 2008. Semin. Immunol. 20, 86.

Arora, K., 2012. Cochlear Implant Stimulation Rates and Speech Perception, in: Modern Speech Recognition Approaches with Case Studies. IntechOpen.

Bas, E., Goncalves, S., Adams, M., Dinh, C.T., Bas, J.M., Van De Water, T.R., Eshraghi, A.A., 2015. Front. Cell. Neurosci. 9, 303.

Bennion, D.M., Horne, R., Peel, A., Reineke, P., Henslee, A., Kaufmann, C., Guymon, C.A., Hansen, M.R., 2021. Otol. Neurotol. 42, 1476–1483.

Carnicer-Lombarte, A., Chen, S.T., Malliaras, G.G., Barone, D.G., 2021. Front. Bioeng. Biotechnol. 9, 622524.

Chandorkar, Y., Ravikumar, K., Basu, B., 2019. ACS Biomater. Sci. Eng. 5, 19–44.

Chen, A., Chen, D., Lv, K., Li, G., Pan, J., Ma, D., Tang, J., Zhang, H., 2022. Adv. Healthc. Mater. 2200807.

Dencker, F., Dreyer, L., Müller, D., Zernetsch, H., Paasche, G., Sindelar, R., Glasmacher, B., 2017. J. Biomed. Mater. Res. B. Appl. Biomater. 105, 2574–2580.

Dorčák, V., Ostatná, V., Paleček, E., 2013. Electrochem. commun. 31, 80–83.

Duan, Y.Y., Clark, G.M., Cowan, R.S.C., 2004. Biomaterials 25, 3813–3828.

Edwards, C.A., Kouzani, A., Lee, K.H., Ross, E.K., 2017. Mayo Clin. Proc. 92, 1427–1444.

Erathodiyil, N., Chan, H.M., Wu, H., Ying, J.Y., 2020. Mater. Today 38, 84–98.

Estephan, Z.G., Schlenoff, P.S., Schlenoff, J.B., 2011. Langmuir 27, 6794–6800.

Farcas, M., Cosman, N.P., Ting, D.K., Roscoe, S.G., Omanovic, S., 2010. J. Electroanal. Chem. 649, 206–218.

Frampton, J.P., Hynd, M.R., Shuler, M.L., Shain, W., 2010. Ann. Biomed. Eng. 38, 1031–1047.

Gao, B., Su, L., Tong, Y., Guan, M., Zhang, X., 2014. J. Phys. Chem. B 118, 12781–12787.

Golabchi, A., Wu, B., Cao, B., Bettinger, C.J., Cui, X.T., 2019. Biomaterials 225, 119519.

Greve, D.W., Huang, X., Nguyen, D., Domach, M.M., 2003. Proc. IEEE Sensors 2, 1358–1363.

Gwon, T.M., Min, K.S., Kim, J.H., Oh, S.H., Lee, H.S., Park, M.H., Kim, S.J., 2015. Biomed. Microdevices 2015 172 17, 1–12.

Harris, A.R., Carter, P., Cowan, R., Wallace, G.G., 2021. ChemElectroChem 8, 1078–1090.

Harris, A.R., Newbold, C., Stathopoulos, D., Carter, P., Cowan, R., Wallace, G.G., 2022. Micromachines 13.

Jorcin, J.B., Orazem, M.E., Pébère, N., Tribollet, B., 2006. Electrochim. Acta 51, 1473–1479.

Kolaya, E., Firestein, B.L., 2021. Biotechnol. Prog. 37, e3179.

Kuang, J., Messersmith, P.B., 2012. Langmuir 28, 7258–7266.

Kwon, I.S., Kim, Y.J., Klosterman, L., Forssell, M., Fedder, G.K., Bettinger, C.J., 2016. J. Mater. Chem. B 4, 3031–3036.

Leigh, B.L., Cheng, E., Xu, L., Andresen, C., Hansen, M.R., Guymon, C.A., 2017. Biomacromolecules 18, 2389–2401.

Lentz, J.J., Van Wijk, E., De Vrieze, E., Parys, Q.-A., Bulck, P. Van, Loos, E., Verhaert, N., 2022. Biomol. 2022, Vol. 12, Page 529 12, 529.

Li, Y., Rehbock, C., Nachev, M., -, A., Newbold, C., Richardson, R., Millard, R., Huang, C., Milojevic, D., Shepherd, R., Cowan, R., 2010. J. Neural Eng 7, 56011–56022.

Liu, Q., Chiu, A., Wang, L.-H., An, D., Zhong, M., Smink, A.M., de Haan, B.J., de Vos, P., Keane, K., Vegge, A., Chen, E.Y., Song, W., Liu, W.F., Flanders, J., Rescan, C., Grunnet, L.G., Wang, X., Ma, M., 2019. Nat. Commun. 10, 5262.

Liu, Y., Ai, K., Lu, L., 2014. Chem. Rev. 114, 5057–5115.

Lysaght, A.C., Kao, S.Y., Paulo, J.A., Merchant, S.N., Steen, H., Stankovic, K.M., 2011. J. Proteome Res. 10, 3845.

Neuburger, J., Lenarz, T., Lesinski-Schiedat, A., Bchner, A., 2009. Int. J. Audiol. 48, 233–239.

Newbold, C., Richardson, R., Huang, C.Q., Milojevic, D., Cowan, R., Shepherd, R., 2004. J. Neural Eng. 1, 218–227.

Quesnel, A.M., Nakajima, H.H., Rosowski, J.J., Hansen, M.R., Gantz, B.J., Nadol, J.B., 2016. Hear. Res. 333, 225–234.

Rebscher, S.J., Hetherington, A., Bonham, B., Wardrop, P., Whinney, D., Leake, P.A., 2008. J. Rehabil. Res. Dev. 45, 731.

Risi, F., 2018. J. Int. Adv. Otol. 14, 382.

Riss, D., Hamzavi, J.S., Blineder, M., Flak, S., Baumgartner, W.D., Kaider, A., Arnoldner, C., 2016. Otol. Neurotol. 37, 882–888.

Ryu, J.H., Messersmith, P.B., Lee, H., 2018. ACS Appl. Mater. Interfaces 10, 7523–7540.

Stathopoulos, D., Chambers, S., Enke, Y.L., Timbol, G., Risi, F., Miller, C., Cowan, R., Newbold, C., 2014. Cochlear Implants Int. 15, 254–263.

Suprun, E. V., 2021. Electrochem. commun. 125, 106983.

Suprun, E. V., Khmeleva, S.A., Radko, S.P., Kozin, S.A., Archakov, A.I., Shumyantseva, V. V., 2016. Electrochem. commun. 65, 53–56.

Thermo Fisher, 2012. Chemical Reactivity of Crosslinkers and Modification Reagents, in: Crosslinking Technology Reactivity Chemistries, Applications and Structure References. pp. 3–4.

Tougaard, S., 2021. J. Vac. Sci. Technol. A 39, 011201.

Upadhye, S., Kumbhare, D., 2018. Am. J. Phys. Med. Rehabil. 97, 72–74.

Vatsyayan, R., Cleary, D., Martin, J.R., -, A., Chen, K.H., Dammann, J.F., Boback, J.L., Newbold, C., Richardson, R., Millard, R., Seligman, P., Cowan, R., Shepherd, R., 2011. J. Neural Eng 8, 36029–36042.

Wilk, M., Hessler, R., Mugridge, K., Jolly, C., Fehr, M., Lenarz, T., Scheper, V., 2016. PLoS One 11, e0147552.

Wright, J.E.I., Fatih, K., Brosseau, C.L., Omanovic, S., Roscoe, S.G., 2003. J. Electroanal. Chem. 550–551, 41–51.

Wu, J., Deng, Y., Kumar, P., Di Mauro, E., Josberger, E., Sayago, J., Pezzella, A., Soavi, F., Cicoira, F., Rolandi, M., Santato, C., 2015. Chem. Mater 27, 58.

Yang, Q., Wu, B., Eles, J.R., Vazquez, A.L., Kozai, T.D.Y., Cui, X.T., 2020. Adv. Biosyst. 4, 1900287.

Yao, R., Wang, J., Li, X., Jung Jung, D., Qi, H., Kee, K.K., Du, Y., 2014. Small 10, 4311–4323.

Zhang, H., Stark, G., Reiss, L., 2015. Otol. Neurotol. 36, 1157.

Zhang, Y., Liu, Y., Ren, B., Zhang, D., Xie, S., Chang, Y., Yang, J., Wu, J., Xu, L., Zheng, J., 2019. J. Phys. D. Appl. Phys. 52, 403001.